

# Role of lattice structure and low temperature resistivity on fast electron beam filamentation in carbon

R. J. Dance<sup>1</sup>, N. M. H. Butler<sup>1</sup>, R. J. Gray<sup>1</sup>, D. A. MacLellan<sup>1</sup>, D. R. Rusby<sup>1,2</sup>,  
G. G. Scott<sup>2</sup>, B. Zielbauer<sup>3</sup>, V. Bagnoud<sup>3</sup>, H. Xu<sup>1</sup>, A. P. L. Robinson<sup>2</sup>, M. P.  
Desjarlais<sup>4</sup>, D. Neely<sup>2,1</sup>, and P. McKenna<sup>1</sup>

<sup>1</sup>Department of Physics, SUPA, University of Strathclyde, Glasgow G4 0NG, UK

<sup>2</sup>Central Laser Facility, STFC Rutherford Appleton Laboratory, Oxfordshire  
OX11 0QX, UK

<sup>3</sup>PHELIX Group, GSI Helmholtzzentrum fuer Schwerionenforschung GmbH,  
D-64291 Darmstadt, Germany

<sup>4</sup>Sandia National Laboratories, P.O. Box 5800, Albuquerque, New Mexico 87185,  
USA

September 20, 2015

E-mail: paul.mckenna@strath.ac.uk

## Abstract

The influence of low temperature (eV to tens-of-eV) electrical resistivity on the onset of the filamentation instability in fast electron transport is investigated in targets comprising of layers of ordered (diamond) and disordered (vitreous) carbon. It is shown experimentally and numerically that the thickness of the disordered carbon layer influences the degree of filamentation of the fast electron beam. Strong filamentation is produced if the thickness is of the order of  $60\text{ }\mu\text{m}$  or greater, for an electron distribution driven by a sub-picosecond, mid- $10^{20}\text{ Wcm}^{-2}$  laser pulse. It is shown that the position of the vitreous carbon layer relative to the fast electron source (where the beam current density and background temperature are highest) does not have a strong effect because the resistive filamentation growth rate is high in disordered carbon over a wide range of temperatures up to the Spitzer regime.

# 1 Introduction

Understanding the transport of large currents of relativistic electrons in dense plasma is not only of fundamental interest but is also important for a wide range of applications of high power lasers. These include the generation of intense x-ray [1, 2] and ion [3, 4] sources, the production of transient states of warm dense matter (WDM) [5, 6] and the fast ignition approach to inertial fusion [7].

Electrical resistivity is known to play a key role in defining the properties of fast electron beam transport in solids. It determines the extent of energy losses through Ohmic heating [8, 9, 10] and drives the self-generation of strong resistive magnetic fields which can lead to beam filamentation (e.g. via resistive instabilities [11]) and change the beam divergence [12]. In previous work we have shown that the electrical resistivity at low temperatures, in the few-to-tens of eV range, has a defining role in establishing the degree of filamentation of the beam [13, 14] and the onset of annular transport patterns [15, 16, 17]. Gradients in resistivity at the interface of two materials [18, 19], in materials subjected to cylindrical shocks [20] and in targets heated using laser-accelerated proton beams [21] have also been shown to play an important role via defining the spatial-magnitude distribution of resistive magnetic fields. Of particular relevance to the present paper is our study of the role of target lattice structure in determining the electrical resistivity at low temperature, which involved an experimental and numerical investigation of fast electron transport in various forms (allotropes) of carbon [13]. The fast electron pulse duration is shorter than the temperature equilibration time between the heated background electrons and initially cold ions within the material. As a result, the fast electrons are transported whilst the material is in a transient state of WDM in which the background ions temporarily retain their initial positions. The degree of initial order in the ionic structure thus defines the evolving material electrical resistivity,  $\eta$ , and by extension the main fast electron beam transport properties.

In this paper, we report on a follow-on experimental and numerical investigation of the role of lattice structure in defining the onset of the filamentation instability in carbon targets. In particular, we investigate fast electron transport in double-layer targets comprising of diamond (ordered) and vitreous (disordered) carbon in various thickness combinations. The thickness of the vitreous carbon propagation layer is shown to affect the beam filamentation pattern, with strong filamentation observed for thicknesses of  $\sim 60 \mu\text{m}$  or greater. The results are discussed with reference to linear resistive instability theory.

## 2 Experiment

Using the PHELIX high power laser at GSI in Darmstadt, S-polarised light with a central wavelength equal to  $1.053\text{ }\mu\text{m}$  was delivered in pulses with duration  $(725\pm100)\text{ fs}$  and energy  $(180\pm10)\text{ J}$ . The beam was focussed using an  $f/1.5$  off-axis parabola into a  $2.5\text{ }\mu\text{m}$  diameter (FWHM) spot, resulting in calculated peak intensity of  $\sim 7\times10^{20}\text{ Wcm}^{-2}$ , at the front side of the target sample.

The targets were either single material or double layer carbon samples (vitreous carbon and diamond), all with total thickness  $L=200\text{ }\mu\text{m}$ . The double layer targets had equal thickness ( $100\text{ }\mu\text{m}$ ) layers of vitreous carbon and diamond pressed together with an ultrathin layer of adhesive. The double-layer targets were irradiated with the layers reversed on alternative shots.

The fast electron transport across the  $L=200\text{ }\mu\text{m}$  targets was diagnosed by measuring the spatial-intensity distribution of the beam of multi-MeV protons accelerated by the fast-electron-generated sheath field formed at the target rear surface. The proton beam distribution is sensitive to modulations in the sheath field produced by variations in the density distribution of fast electrons arriving at the target rear side. The approach is discussed in references [14, 22, 23, 24]. The measurements were made using stacked dosimetry (radiochromic, RCF) film positioned 5 cm from the target. The stack configuration enabled proton energies beyond 40 MeV to be detected. The maximum measured energy was 36 MeV. Figure 1(a) shows a schematic of the arrangement.

Figures 2(a) and (b) show representative measured spatial-intensity distributions (at an example energy of 10 MeV) of the beam of protons accelerated from  $200\text{ }\mu\text{m}$ -thick samples of vitreous carbon and diamond, respectively. In agreement with similar results presented in reference [13], the disordered form of carbon produces a proton beam with significant cusp-like modulations, reflecting modulation of the fast electron distribution due to transport instabilities. By contrast, the proton beam produced with diamond is smooth, except for a localised region of structure near the centre (as also observed previously [14] using the Vulcan laser at the Rutherford Appleton Laboratory).

The equivalent measurements for the double layer targets, corresponding to vitreous carbon-diamond (100VC/100D) and diamond-vitreous carbon (100D/100VC) are shown in figures 2(c) and (d), respectively. Each layer is  $100\text{ }\mu\text{m}$ -thick, such that  $L=200\text{ }\mu\text{m}$  for all targets. In both cases evidence of filamentation is observed, but to differing degrees. The cusp-like structures in the proton beam are larger when vitreous carbon is at the target front layer compared to the reverse case.

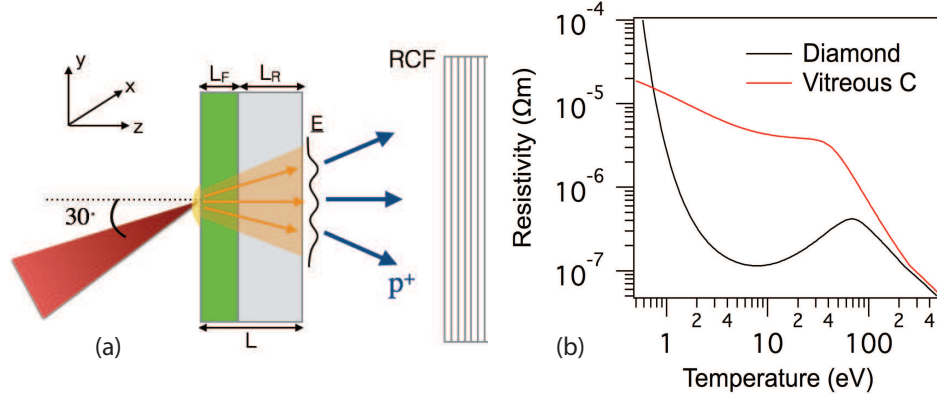


Figure 1: (a) Schematic illustrating the experiment arrangement.  $L_F$  and  $L_R$  correspond to the thickness of the front and rear layers, respectively, in the double layer targets. The RCF film stack measures the spatial-intensity distribution of the beam of protons accelerated from the target rear side. (b) Electrical resistivity as a function of temperature for disordered (vitreous) and ordered (diamond) forms of carbon. These  $\eta$ - $T$  profiles were calculated using quantum molecular dynamics simulations coupled with the Kubo-Greenwood approach, as discussed in reference [13].

### 3 Modelling

To investigate the underlying electron transport physics, the 3D Zephyros hybrid-PIC code [26] is used to simulate the transport of fast electrons within single and double-layer carbon targets. In this approach, the fast electron population is described kinetically using the Vlasov equation, which is solved via the PIC method and the background electrons are treated as a fluid. Collisions are included using the Fokker-Planck collisional operators [27] and include drag generated by the background electrons. Energy deposition due to the slowing down of the fast electrons and Ohmic heating induced by the return current are used to determine the temperature evolution within the target. The electrical resistivity,  $\eta$ , as a function of temperature,  $T$ , for both diamond and vitreous carbon is plotted in figure 1(b). These  $\eta$ - $T$  plots were obtained from a series of detailed quantum molecular dynamics simulations using the VASP plane-wave density functional theory. The atomic configurations sampled as a function of temperature were used in subsequent wide-ranging Kubo-Greenwood resistivity calculations [28, 29], as described in reference [13]. The significantly higher resistivity of vitreous carbon compared to diamond over the temperature range from a few eV up to the Spitzer temperature of  $\sim 80$  eV [30] gives rise to filamented fast electron transport in the disordered form of carbon, as discussed in reference [13].

The same grid is used for all the simulations and is  $400 \mu\text{m} \times 400 \mu\text{m} \times 200 \mu\text{m}$ , with cell

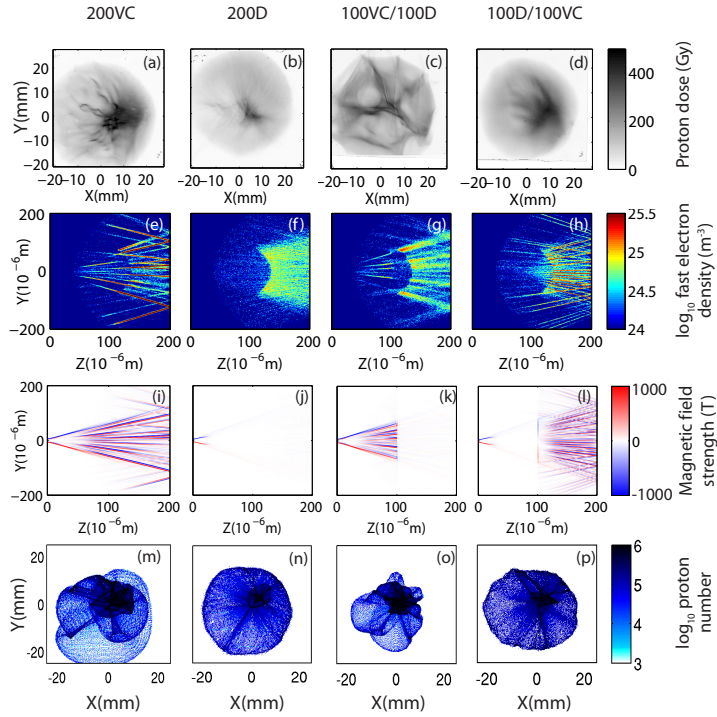


Figure 2: TOP ROW: Measured proton spatial-intensity dose profiles (Gy) for: (a)  $L=200$   $\mu\text{m}$  vitreous carbon; (b)  $L=200$   $\mu\text{m}$  diamond; (c)  $L_F=100$   $\mu\text{m}$  vitreous carbon and  $L_R=100$   $\mu\text{m}$  diamond; (d)  $L_F=100$   $\mu\text{m}$  diamond and  $L_R=100$   $\mu\text{m}$  vitreous carbon; SECOND ROW: Corresponding  $\log_{10}$  fast electron density maps ( $\text{m}^{-3}$ ) in the [Y-Z] plane, from 3D Zephyros hybrid-PIC simulations, at 1.2 ps from the start of the electron injection; THIRD ROW: Corresponding [Y-Z] mid-plane 2D maps of the magnetic flux density ( $B_x$  component in Tesla); BOTTOM ROW: Corresponding modelled proton spatial-intensity maps, calculated using the rear-side fast electron density maps obtained from (e)-(h).

size equal to  $\Delta X = \Delta Y = \Delta Z = 1$   $\mu\text{m}$ . A total of  $2 \times 10^8$  macro-particles are injected over a 725 fs pulse duration. The side boundaries are transmissive for all simulations to avoid any potential artificial effects due to the transverse size of the simulation box and the rear boundary is reflective to mimic the reflection effect on the fast electrons of the sheath field formed on the target rear surface. The simulation outputs are sampled just after the bulk of the fast electrons have reached the rear boundary (after 1.2 ps) and therefore the reflected electrons have little effect on the main fast electron transport pattern. The choice of a 200  $\mu\text{m}$ -thick target also ensures that fast electron refluxing is minimised in the experiment. The background temperature is initialised at 1 eV.

Electrons are injected at  $[X, Y, Z] = [0, 0, 0]$ , uniformly over a cone with half-angle equal to

40° [31]. The electrons have an exponential energy distribution,  $\exp(-E_f/kT_f)$ , where  $E_f$  is the electron kinetic energy and  $kT_f$  is the product of Boltzmann's constant and the fast electron temperature. The latter is determined assuming ponderomotive scaling [32]. The total electron energy is determined assuming 30% conversion efficiency from the laser pulse energy to fast electrons. This value was chosen based on previous investigations of energy absorption and coupling to electrons for similar laser pulse parameters. For example, the conversion efficiency was found to be in the range 15% - 30% at the slightly lower peak intensity of  $4 \times 10^{20} \text{ Wcm}^{-2}$  in reference [33].

Results from the simulations for parameters matched to the experiment are shown in figures 2(e)-(l). 2D fast electron density maps in the [Y-Z] plane at  $X=0$  are shown in figures 2(e)-(h) and the corresponding self-generated, resistive magnetic field distributions are shown in figures 2(i)-(l). Considering first the two single layer targets, strongly filamented transport is predicted for vitreous carbon and smooth beam transport for diamond. These results are in good qualitative agreement with the measurements of the proton beam profile shown in figures 2(a) and (b), respectively. The rear-surface fast electron density distribution results from the Zephyros simulations are used to compute the evolution of the 2D sheath field at the target rear surface and the spatial-intensity distribution of the resulting beam of protons, using the approach described in references [14, 24]. Figures 2(m) and (n) show the predicted proton beam distributions for vitreous carbon and diamond, respectively, and are in good qualitative agreement with the corresponding proton beam measurements. The profile for diamond is generally smooth with a small degree of structure at the centre and clear cusp-like features are predicted for vitreous carbon, which are similar to those measured in figure 2(a).

The simulation and model results for the double-layer targets are also in good qualitative agreement with experiment. In both double-layer configurations, strong filamentation occurs within the vitreous carbon layer. When this layer is at the target rear (right hand column of figure 2), a large number of small filaments are produced over the full layer thickness and reach the target rear side. By contrast, when the vitreous carbon layer is at the target front side the beam starts to filament only after a depth of  $\sim 30 \mu\text{m}$  due to the low resistivity in the high temperature Spitzer regime at the source. A smaller number of filaments are produced as a result. As the resistive magnetic fields formed around the filaments are weaker in the diamond layer some degree of broadening and merging of the filaments occur as they propagate. These processes result in few, but larger radii filaments reaching the target rear side. These simulation results are consistent with the measurements, particularly for the latter case in which the proton beam contains large cusp like structures, as shown in figure 2(c).

We note that measurement of the degree of structure in the proton beam enables the onset of filamentation in the fast electron transport to be diagnosed and works well when a relatively small number of separated filaments reach the target rear. When the filamentation instability results in a large number of filaments in close proximity, transverse spreading of the fast electron current on the rear surface [25] can act to decrease the modulations in the sheath field on the time scale of the proton acceleration. This renders the diagnostic technique less sensitive to fine-scale filamentary structure. The presence of finer cusp-like structures in the proton beam in figure 2(a) compared to figure 2(c) indicates a larger number of filaments in the electron transport. However, the very fine and closely spaced filaments in figure 2(h) are more difficult to diagnose via proton acceleration. A further discussion on the role of fast electron transverse spreading at the target rear surface and its influence on the measured proton beam can be found in reference [14].

In order to quantify and compare the degree of filamentation of the fast electron beam in the simulations with the structure in the measured proton dose the following method is applied. The density distribution of the fast electron beam at the target rear surface is first transformed into polar coordinates  $[r, \theta]$ , where  $r=0$  is the beam centre. The densities along  $r$  are then extracted for  $0 \leq \theta \leq 360^\circ$  in  $1^\circ$  increments (i.e. 360 radial line-outs). The root mean square deviation (RMSD) with respect to the average beam density is calculated and the average over all angles determined to produce a single deviation quantity,  $\bar{S}$ . The procedure is repeated for five time steps in the simulation (centred around 1.2 ps) and the final  $\bar{S}$  data point plotted in figure 3 is the mean, and the error bars the standard deviation, of the five sample simulation results. The same approach is then applied to quantify the variation in the proton dose as measured using the RCF. The technique will be described in more detail in a future publication.

The degree of variation in the measured proton dose across the four target types is in good agreement with the degree of fast electron beam filamentation (determined from the fast electron density variation), as shown in figure 3(a). Note the different y-axes for the two data sets. The degree of change in the cusp-like structure measured in the proton beam is clearly correlated to the degree of change in the filamentation predicted in the fast electron transport. We note that this approach is particularly sensitive at quantifying the degree of small scale structure and thus a relatively high  $\bar{S}$  value is obtained for the targets with vitreous carbon at the rear side (i.e. 200VC and 100D/100VC).



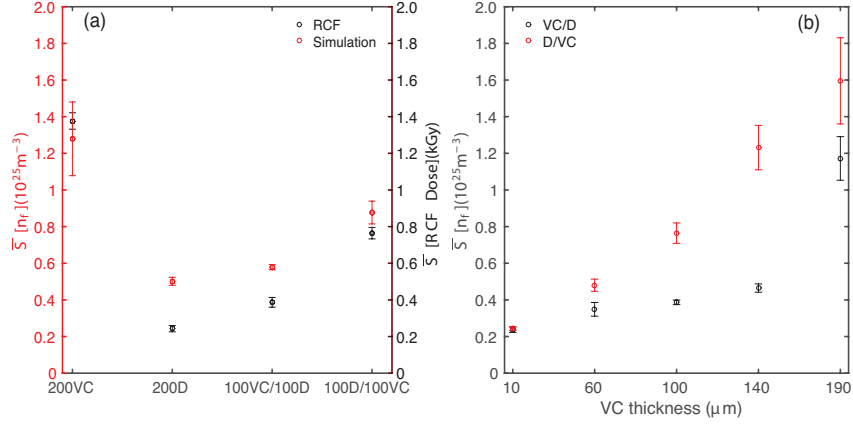


Figure 3: (a) Variation in the rear surface fast electron density in the simulation results (left axis) and the measured proton dose (right axis) for the four given target types; (b) Variation in the fast electron density as a function of the thickness of the vitreous carbon layer, both for the layer at the front and at the rear. Details of the methodology are given in the text.

## 4 Variation of the vitreous carbon layer thickness

In the last section we demonstrated that irrespective of whether the vitreous carbon layer is positioned at the front or rear of the target it will induce filamentation instability in the fast electron beam. In this section, we investigate the sensitivity of the fast electron beam filamentation to the thickness of the vitreous carbon layer.

Firstly, a series of simulation runs were performed with the same fast electron injection properties discussed above and for the same total target thickness  $L=200 \mu\text{m}$ , but with the thickness of the front, vitreous carbon layer varied between  $L_F=10 \mu\text{m}$  and  $190 \mu\text{m}$ . The rear surface layer is diamond in each case. The results are shown in figure 4, in which (a)-(e) corresponds to the fast electron density, (f)-(j) is the corresponding resistive magnetic field, and (k)-(p) is the corresponding electrical resistivity, all in the [Y-Z] mid-plane. Generally, as the thickness of the vitreous carbon layer is increased, going from left to right in figure 4, an increased degree of filamentation is observed. For the cases  $L_F < 50 \mu\text{m}$  the fast electron transport pattern is relatively smooth. For  $L_F \sim 50\text{-}60 \mu\text{m}$  there is evidence of the onset of filamentation, and for larger  $L_F$  the beam is strongly filamented. The fact that there is little or no evidence of beam transport instabilities within the first  $50 \mu\text{m}$  of the electron source is a result of the strong heating within this region, particularly within the first few tens of microns. The resistivity is very low in this region because the target is heated well into the Spitzer regime, for which the resistivity decreases with increasing temperature, as shown in figure 1(b). Figures 4(p)-(t) show

the predicted proton beam distributions as modelled using the fast electron density profile at the target rear from the corresponding simulations. The degree of structure in the beam of accelerated protons is expected to increase with increasing  $L_F$ , and thus measurement of the proton beam spatial-intensity distribution would provide a test of these simulation predictions.

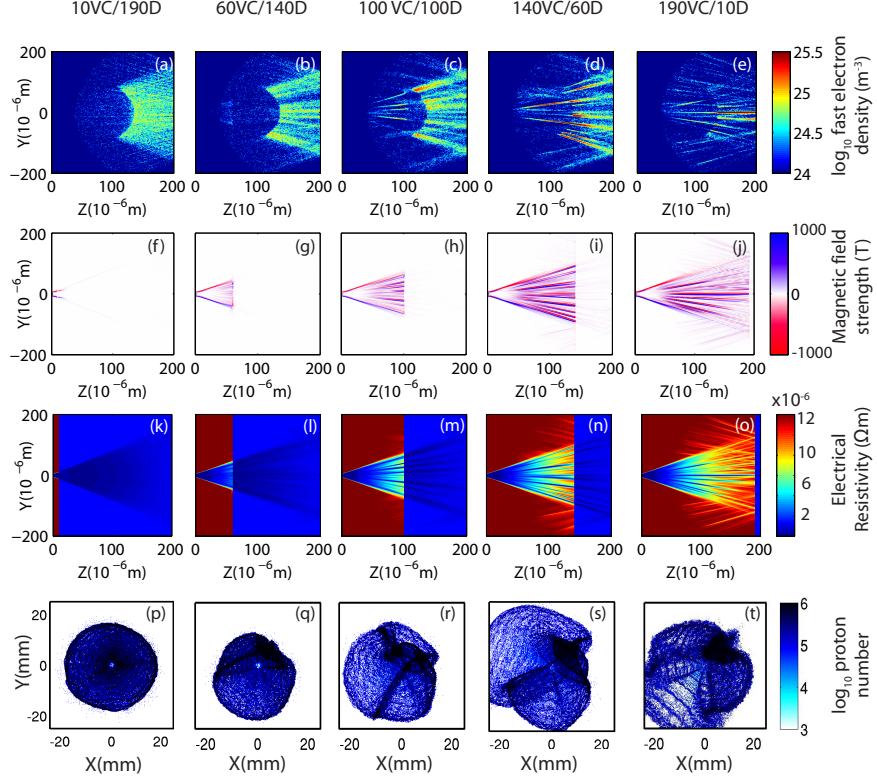


Figure 4: Zephyros simulation results for double layer targets with vitreous carbon as the front layer and diamond as the rear. TOP ROW:  $\text{Log}_{10}$  fast electron density maps ( $\text{m}^{-3}$ ), in the [Y-Z] mid-plane, for: (a)  $L_F=10 \mu\text{m}$ ; (b)  $L_F=50 \mu\text{m}$ ; (c)  $L_F=100 \mu\text{m}$ ; (d)  $L_F=140 \mu\text{m}$ ; (e)  $L_F=190 \mu\text{m}$ ; SECOND ROW: Corresponding 2D maps of the magnetic flux density ( $B_x$  component in Tesla); THIRD ROW: Corresponding 2D maps of electrical resistivity ( $\Omega\text{m}$ ); BOTTOM ROW: Corresponding modelled proton spatial-intensity maps, calculated using the rear-side fast electron density maps obtained from (a)-(e).

Next we perform a series of simulations with the order of the layers reversed, i.e. with diamond at the front and vitreous carbon at the rear. All other conditions are identical to the previous simulations. The results are shown in figure 5. As the thickness of the vitreous carbon layer,  $L_R$ , is decreased from left to right in the figure, a larger density of finer filamentary structure is observed. The overall fast electron beam pattern is filamented less strongly for

$L_R < 60 \mu\text{m}$ . Importantly, as this layer is at the target rear in this series of runs, this thickness threshold for strong filamentation is not connected to the strong heating at the target front side. There are nonetheless differences in the size of filamentary structure depending on whether the vitreous carbon is at the front or rear side. More numerous and finer scale filaments are produced in the latter case and this is reflected in the typically higher values of  $\bar{S}$  shown in figure 3(b).

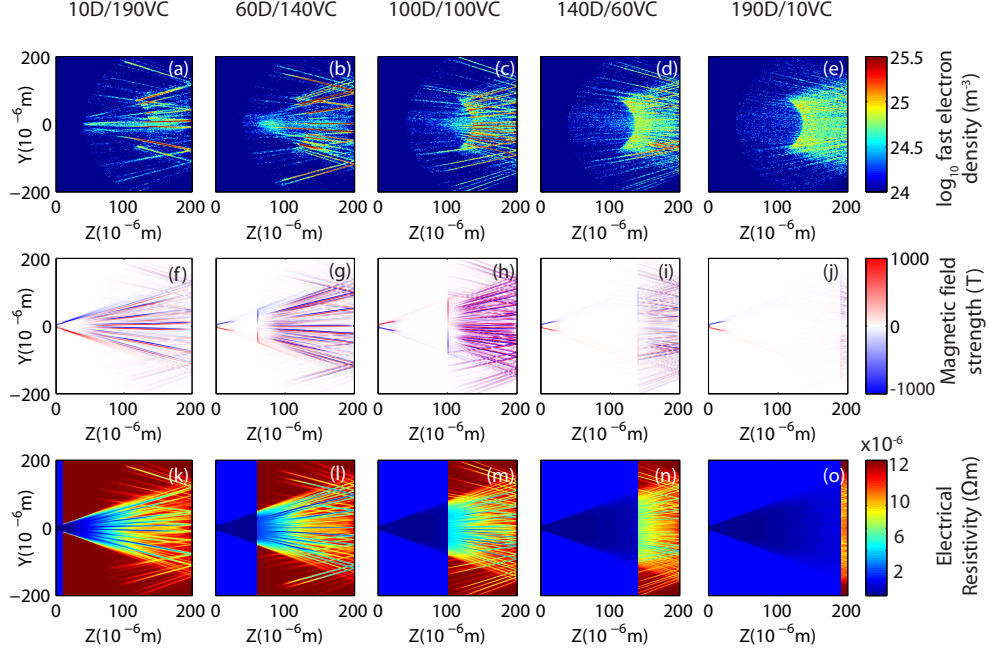


Figure 5: Zephyros simulation results for double layer targets with diamond as the front layer and vitreous carbon as the rear. TOP ROW:  $\text{Log}_{10}$  fast electron density maps ( $\text{m}^{-3}$ ), in the [Y-Z] mid-plane, for: (a)  $L_F = 10 \mu\text{m}$ ; (b)  $L_F = 50 \mu\text{m}$ ; (c)  $L_F = 100 \mu\text{m}$ ; (d)  $L_F = 140 \mu\text{m}$ ; (e)  $L_F = 190 \mu\text{m}$ ; MIDDLE ROW: Corresponding 2D maps of the magnetic flux density ( $B_x$  component in Tesla); BOTTOM ROW: Corresponding 2D maps of electrical resistivity ( $\Omega\text{m}$ ).

Finally, we have also explored the scenario in which the vitreous carbon layer is buried within a target with diamond layers at both the front and rear sides. Example results from this series of simulations are shown in figure 6. In each case we find some degree of filamentation, and that the filaments become more distinct with increasing thickness of the vitreous carbon layer. Fine scale filamentary structure is not observed due to the diamond layer at the target rear side, which (as discussed above) causes the filaments to expand. We note that a transverse magnetic field is induced at the boundaries of the target layers, as observed in figure 6(e)-(h). Previous simulation studies involving buried layers of materials with significantly different atomic number, such as a buried copper layer in a plastic target as considered by Yang *et al.* [34], have concluded

that significant transverse spreading of the fast electron beam can be produced by strong field generation at the interface. The magnitude of this field component in the present work is lower than that produced around the filaments and the azimuthal field produced within the first few tens of microns from the electron source. This transverse field does not appear to affect the beam transport pattern in the present study.

We conclude from these three sets of simulations that although some degree of filamentation is induced if a vitreous carbon layer is present, strong filamentation only occurs if the thickness of this layer is larger than  $\sim 60 \mu\text{m}$ . This is the case independent of the position of the layer, albeit that the final density and size of the filaments is sensitive to the layer position.

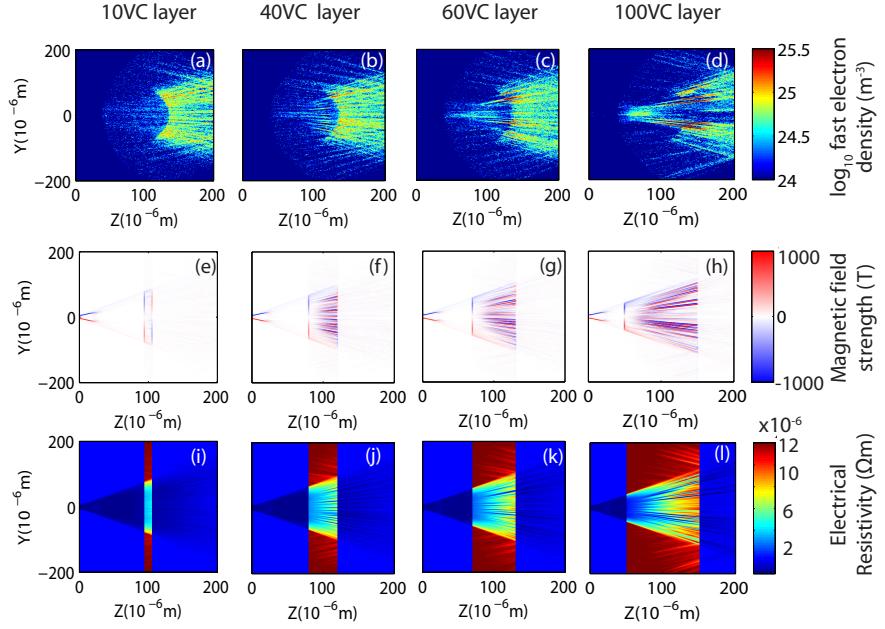


Figure 6: Zephyros simulation results for triple layer targets comprising a vitreous carbon layer at the centre of a diamond target with overall length  $L=200 \mu\text{m}$ . TOP ROW:  $\text{Log}_{10}$  fast electron density maps ( $\text{m}^{-3}$ ), in the [Y-Z] mid-plane, for buried layer thickness of: (a)  $10 \mu\text{m}$ ; (b)  $40 \mu\text{m}$ ; (c)  $60 \mu\text{m}$ ; (d)  $100 \mu\text{m}$ ; MIDDLE ROW: Corresponding 2D maps of the magnetic flux density ( $B_x$  component in Tesla); BOTTOM ROW: Corresponding 2D maps of electrical resistivity ( $\Omega\text{m}$ ).

## 5 Resistive instability growth rate

To explain the dependency of filamentation on the thickness of the vitreous carbon layer and the observation that it is largely independent of the position of the layer within the target, it is instructive to estimate the resistive filamentation growth rate in both carbon allotropes. Although the ionisation instability can also give rise to micron-scale transverse filamentation at solid densities, this occurs in insulator targets for which ionization is needed to provide the electrons for the return current. Since the chemical element (and therefore ionisation potential) is the same in diamond and vitreous carbon, ionisation instability is very unlikely to explain the very different filamentation rates in these two materials. On the other hand, the growth rate of the resistive filamentation depends sensitivity on the target resistivity and the resistivity-temperature profile is the main parameter which differs between diamond and vitreous carbon. Resistive filamentation is therefore considered to be the main candidate to explain the observed results.

A linear resistivity analysis, based on the work of Gremillet *et al.* [11] and Robinson *et al.* [35] is performed. This model has several simplifying assumptions, including uniformity of the background resistivity, and does not take account of the resistivity evolution. Nevertheless it can be used to provide an estimate of the local resistive instability growth rate at a given point in space and time, and importantly, an indication of the relative difference between the growth rates of the two carbon allotropes.

In this approach, the fast electrons are given a fluid description, with the linearised fluid equations presented in reference [35]. The beam filamentation has an exponentially growing mode,  $\exp(\Gamma t)$ , where  $t$  is time and the growth rate  $\Gamma$  is given by [35]:

$$\Gamma = (\alpha/2 + \sqrt{D})^{1/3} - (\sqrt{D} - \alpha/2)^{1/3} \quad (1)$$

where  $D = (\beta/3)^3 + (\alpha/2)^2$ ,  $\alpha = \frac{e^2 u_{x,0}^2 n_{f,0} k_p^2 \eta}{\gamma m_e}$  and  $\beta = \frac{k_p^2 e T_{f,\perp}}{\gamma m_e}$ ,  $k_p = 2\pi/\lambda$  is the wavenumber of the perturbation and  $T_{f,\perp}$  is the beam transverse temperature. The fast electron density,  $n_{f,0}$ , and velocity,  $u_{x,0}$ , are estimated as  $10^{26} \text{ m}^{-3}$  and  $c$  respectively. The reason that the filamentation growth rate is a function of the transverse temperature is that as the instability grows the local magnetic field results in a pinching force, which in the absence of transverse temperature would cause the filaments to continue to collapse. The pressure force provided by the transverse temperature causes the filament to expand and thus the filamentation growth is sensitive to the balance between these opposing forces - a higher transverse temperature results in a lower filamentation growth rate (see reference [36] for a fuller discussion on the role of transverse temperature in stabilising transverse instability growth).

Firstly, the scale of the difference in the instability growth rate in the two allotropes of carbon is considered, with reference to figure 7(a) (other parts of this figure are discussed in subsequent paragraphs), which shows  $\Gamma$  as a function of  $k_p$  for both materials at three example beam transverse temperatures. An average value over the temperature range 1-50 eV for the resistivities of vitreous carbon and diamond are taken as  $4 \times 10^{-6} \Omega\text{m}$  and  $2 \times 10^{-7} \Omega\text{m}$ , respectively. The resistive filamentation growth rate is significantly higher (about an order of magnitude) in vitreous carbon than in diamond over the full range of beam transverse temperatures and perturbation wavenumbers explored. Thus the beam will filament much faster in the case of disordered carbon. The e-folding time (time for the filamentation to grow by a factor equal to Euler's number) for vitreous carbon varies from 10 to 100 fs across the range of  $k_p$  values considered for  $T_{f,\perp} = 20$  keV, for example. The propagation length of  $\sim 60 \mu\text{m}$  in vitreous carbon needed to observe strong filamentation in the simulations above corresponds to a propagation time of  $\sim 200$  fs for relativistic electrons. This is consistent with several e-foldings, as may be expected for strong fast electron beam filamentation to occur.

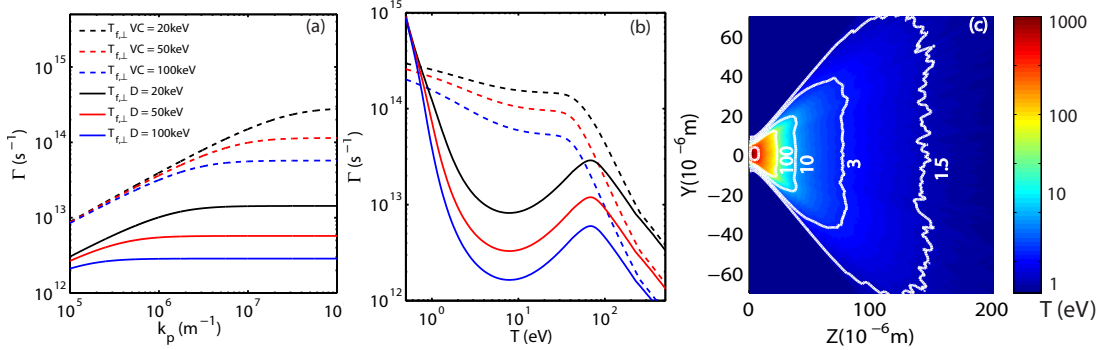


Figure 7: Resistive instability growth rate as a function of (a) wave number and (b) temperature, for vitreous carbon (VC) and diamond (D), at three example beam transverse temperatures (given). The dashed lines correspond to vitreous carbon and the solid lines are for diamond; (c) Example 2D temperature map (eV) in the Y-Z mid-plane at 1.2 ps. Contours are drawn for isothermals corresponding to 1.5, 3, 10 and 100 eV.

Next, the resistive filamentation growth rate is calculated for both carbon allotropes as a function of temperature, using the  $\eta$ - $T$  profiles shown in figure 1. The results, plotted in figure 7(b), show that the resistive instability growth rate in vitreous carbon is much higher than in diamond over the temperature range from  $\sim 1$  eV to the start of the Spitzer regime at  $\sim 80$  eV. Figure 7(c) shows a typical 2D map of the electron temperature within a diamond target 1.2 ps into the simulation. This plot serves to illustrate that, apart for the first few tens of microns

in the region of the fast electron source where the target is heated to Spitzer temperatures, over most of the rest of the propagation length the temperature is in the range  $1 \leq T[\text{eV}] \leq 80$ . The resistivity of vitreous carbon is high over this full temperature range, as shown in figure 7(b). Therefore, to a first approximation, the position of the vitreous carbon layer within the 200  $\mu\text{m}$ -thick target (after the first few tens of microns) has little effect on the overall degree of filamentation.

## 6 Summary

In summary, the transverse filamentation instability of a beam of fast electrons has been investigated in ordered and disordered allotropes of carbon and as a function of the thickness and position of a disordered layer in multi-layered samples. We note that the experimental results with single layer targets reported here, obtained with the PHELIX laser at GSI, are consistent with the results obtained using the same diagnostic approach using the Vulcan laser and reported in reference [13]. The peak laser intensity is similar in both experiments (mid- $10^{20} \text{ Wcm}^{-2}$ ), although the pulse duration, energy and focal spot sizes are all slightly smaller in the present study.

The new features of the present results are the demonstration of the sensitivity of the beam filamentation to the thickness of the vitreous carbon layer and its position with respect to the electron source. Strong filamentation is observed when the thickness is of the order of  $\sim 60 \mu\text{m}$  or higher. This is shown to be consistent with predictions of a simple linear resistive instability model, which also accounts for the differences in the filamentation observed in the two allotropes of carbon. With the exception of the immediate vicinity of the electron source where the temperature is high, filamented transport is produced irrespective of the position of the vitreous carbon layer. This reflects the high and slowly varying filamentation growth rate with temperature for vitreous carbon in the WDM temperature regime throughout the bulk of the target volume.

## 7 Acknowledgements

We gratefully acknowledge the PHELIX laser group at GSI and the use of computing resources provided by STFC's e-Science project. This work is financially supported by EPSRC (grant numbers EP/J003832/1 and EP/K022415/1), STFC (grant number ST/K502340/1), LASERLAB-EUROPE (grant agreement no. 284464, EC's Seventh Framework Programme) and the Air Force Office of Scientific Research, Air Force Material Command, USAF, under grant num-

## References

- [1] M. D. Perry *et al.*, Rev. Sci. Instrum. **70**, 265 (1999)
- [2] C. D. Chen *et al.*, Phys. Plasmas **16**, 9 (2009)
- [3] H. Daido, M. Nishiuchi and A.S. Pirozhkov, Rep. Prog. Phys., **75**, 056401 (2012)
- [4] A. Macchi, M. Borghesi and M. Passoni, Rev. Mod. Phys., **85**, 751 (2013)
- [5] L. B. Fletcher *et al.*, Nature Photonics **9**, 274 (2015)
- [6] O. Ciricosta *et al.*, Phys. Rev. Lett. **109**, 065002 (2012)
- [7] M. Tabak *et al.*, Phys. Plasmas **1**, 1626 (1994)
- [8] M. H. Key *et al.*, Physics of Plasmas, **6** 1966, (1988)
- [9] R. R. Freeman *et al.*, Fus. Sci. Technol. **49**, 297 (2006)
- [10] X. Vaisseau *et al.*, Phys. Rev. Lett. **114**, 095004 (2015)
- [11] L. Gremillet *et al.*, Phys. Plasmas **9**, 941 (2002)
- [12] A. R. Bell and R. J. Kingham, Phys. Rev. Lett., **91**, 035003 (2003)
- [13] P. McKenna *et al.*, Phys. Rev. Lett., **106**, 185004 (2011)
- [14] D. A. MacLellan *et al.*, Laser Part. Beams **31**, 475 (2013)
- [15] D. A. MacLellan *et al.*, Phys. Rev. Lett., **111**, 167588 (2013)
- [16] D. A. MacLellan *et al.*, Plasma Phys. Contr. Fusion, **56**, 084002 (2014)
- [17] P. McKenna *et al.*, Plasma Phys. Control. Fusion **57**, 064001 (2015)
- [18] S. Kar *et al.*, Phys. Rev. Lett. **102**, 055001 (2009)
- [19] B. Ramakrishna *et al.*, Phys. Rev. Lett. **105**, 135001 (2010)
- [20] F. Perez *et al.*, Phys. Rev. Lett. **107**, 065004 (2011)
- [21] D. A. MacLellan *et al.*, Phys. Rev. Lett., **113**, 185001 (2014)



- [22] J. Fuchs *et al.*, Phys. Rev. Lett., **91**, 255002 (2003)
- [23] X. H. Yuan *et al.*, New Journal of Physics **12**, 063018 (2010)
- [24] M. N. Quinn *et al.*, Plasma Phys. Control. Fusion **53**, 025007 (2011)
- [25] P. McKenna *et al.*, Phys. Rev. Lett., **98**, 145001 (2007)
- [26] A. P. L. Robinson *et al.*, Phys. Rev. Lett., **108**, 125004 (2012)
- [27] A. G. R. Thomas *et al.*, J. Comput. Phys., **231**, 1051 (2012)
- [28] M. P. Desjarlais, J. D. Kress, and L. A. Collins, Phys. Rev. E **66**, 025401 (2002).
- [29] G. Kresse and J. Hafner, Phys. Rev. B **47**, 558 (1993)
- [30] L. Spitzer and R. Harm, Phys. Rev., **89**, 5 (1953)
- [31] M. Coury *et al.*, Phys. Plasmas **20**, 043104 (2013)
- [32] S. C. Wilks and W. L. Kruer, IEEE J. Quantum Electron. **33**, 1954 (1997)
- [33] M. Nakatsutsumi *et al.*, New Journal of Physics **10**, 043046 (2010)
- [34] X. H. Yang *et al.*, Plasma Phys. Control. Fusion, **57**, 025011 (2015)
- [35] A. P. L. Robinson *et al.*, Plasma Phys. Control. Fusion, **50**, 065019 (2008)
- [36] L. O. Silva *et al.*, Phys. Plasmas **9**, 2458 (2002)